J Mater Sci (2026) 61:18341–18359

Polymers & biopolymers

Antifouling and antibacterial PES ultrafiltration membranes fabricated using an unmodified 3D printer-assisted casting platform

Ahmet Aydın[1], Fatma Demirci[1], Mehmet Orhan[2], and Hasan Basri Kocer[1,*]

[1] *Department of Polymer Materials Engineering, Faculty of Engineering and Natural Sciences, Bursa Technical University, Bursa, Turkey*
[2] *Faculty of Engineering, Textile Sciences, Textile Engineering, Bursa Uludag University, Bursa, Turkey*

Received: 15 January 2026
Accepted: 27 April 2026
Published online: 13 May 2026

© The Author(s), 2026

ABSTRACT

In this study, the fabrication of ultrafiltration membranes is reported through the innovative use of a commercial, unmodified 3D printer, which was utilized not as a printing tool but as a precisely controlled motion and temperature platform. This approach offers a novel, cost-effective, and reproducible alternative to conventional production methods, enabling improved control over fabrication parameters and enhanced reproducibility compared to conventional manual casting methods. Fabrication parameters were systematically optimized, initially by varying the casting temperature (30, 60, and 90 °C) at a fixed speed, and subsequently by modulating the casting speed (32.5, 65, 97.5, and 130 mm s^{-1}) at the predetermined optimal temperature. To impart antifouling and antibacterial functionality, a custom-synthesized *N*-halamine-based polymer was incorporated into the optimized casting solution to create *N*-halamine-modified membranes. The resulting membranes exhibited thicknesses ranging from 103 to 152 µm, with pure water flux values between 60 and 239 L m^{-2} h^{-1} and bovine serum albumin rejection rates consistently exceeding 90%. Notably, the *N*-halamine-modified membrane demonstrated a flux recovery ratio of approximately 109% after chemical washing, significantly surpassing the ~ 73% flux recovery ratio of its unmodified counterpart. Furthermore, the antibacterial assays demonstrated that the chlorinated, modified membrane effectively inactivated both *Staphylococcus aureus* and *Escherichia coli* within 15 min (> 5-log reduction), whereas the control membranes showed no significant antibacterial activity. In addition, porosity and pore size analyses confirmed that the membrane structure was preserved after modification and chemical cleaning, while long-term stability tests indicated stable immobilization of the N-halamine polymer within the membrane matrix. These findings establish a 3D printer-assisted casting approach as a feasible strategy for

Handling Editor: Maude Jimenez.

Address correspondence to E-mail: hasan.kocer@btu.edu.tr

https://doi.org/10.1007/s10853-026-12884-9

membrane fabrication and highlight *N*-halamine incorporation for creating membranes with enhanced and regenerable antifouling and antibacterial performance.

Introduction

Membrane technology is indispensable for liquid concentration and component separation processes [1]. Pressure-driven membrane systems are typically classified based on their nominal pore sizes into microfiltration (MF), ultrafiltration (UF), nanofiltration (NF), and reverse osmosis (RO) [2]. While MF and UF employ porous structures, NF and RO rely on effectively dense matrices for separation. UF membranes, characterized by pore sizes of 1–500 nm and molecular weight cut-offs (MWCOs) of 1–200 kDa, are particularly effective for retaining macromolecules such as proteins, enzymes, bacteria, and viruses, which are poorly rejected by MF systems [3]. These membranes are commonly fabricated with an asymmetric porous structure via phase inversion using polymers such as polyethersulfone (PES), polysulfone (PSf), and polyvinylidene fluoride (PVDF) [4]. The widespread adoption of UF in sectors such as water treatment and bioprocessing is driven by its low energy consumption and environmental compatibility [5].

Despite these advantages, membrane fouling remains a critical bottleneck that severely impairs process efficiency and increases operational costs [2]. This phenomenon, initiated by concentration polarization and the subsequent formation of a foulant layer, can be categorized as reversible, irreversible, or irrecoverable [6]. While reversible fouling can be mitigated by physical cleaning, irreversible fouling requires aggressive chemical cleaning, often involving agents such as sodium hypochlorite, and irrecoverable fouling necessitates complete membrane replacement [7].

A primary cause of fouling is the inherent hydrophobicity of conventional membrane polymers (e.g., PES, PVDF, and PSf), which promotes the adsorption of foulants and leads to pore blockage. Although incorporating hydrophilic additives such as poly(vinylpyrrolidone) (PVP) can enhance wettability, biofouling driven by bacterial adhesion and biofilm formation remains a persistent challenge [3, 7, 8]. This has motivated the development of membranes with intrinsic antibacterial properties. While various biocidal agents have been explored, many suffer from limitations such as nanoparticle leaching or insufficient long-term efficacy [9, 10]. In contrast, *N*-halamine compounds present a robust and regenerable alternative, as their antibacterial activity can be readily restored through contact with a chlorine source [11, 12]. Furthermore, unlike heavy metal-based antimicrobial agents (e.g., silver nanoparticles), polymeric *N*-halamines do not release toxic heavy metal ions into the environment, making them potentially more environmentally favourable [13–16]. However, despite these advantages, several critical challenges remain. The long-term stability of *N*-halamine functionalities within polymer matrices, their potential leaching behaviour, and their influence on membrane structure and separation performance are still under debate [13, 17]. In addition, the incorporation of such functional additives may alter the phase inversion process (Non-solvent Induced Phase Separation, NIPS), leading to changes in pore morphology, porosity, and permeability [18, 19]. Therefore, it is essential to develop fabrication strategies that can integrate antibacterial functionality while maintaining precise control over membrane structure and reproducibility.

In this context, achieving optimal membrane performance depends not only on the surface chemistry but also critically on the physical porous structure, which is dictated by the fabrication conditions. Conventional casting methods often lack the high degree of precision and reproducibility required to finely tune the membrane morphology. While a few studies have explored the use of highly modified or custom-built 3D printers, there remains a lack of research utilizing commercial 3D printers as controllable motion platforms for membrane fabrication [20–23]. To address this gap, the present study introduces a 3D printer-assisted casting system, in which a commercial, unmodified 3D printer is employed not as a printing device, but as a precision-controlled platform enabling accurate regulation of substrate temperature (23–300 ºC, ± 0.1 ºC) and casting speed (1–500, ± 0.1 mm s^{-1}). This approach represents a simple, low-cost, and reproducible alternative to conventional laboratory-scale casting setups, while maintaining full compatibility with NIPS-based membrane formation. Unlike previously reported approaches that rely on modified or specialized printing systems, this study demonstrates that a fully unmodified commercial 3D printer can be effectively repurposed as a precise and

programmable casting platform, providing enhanced control over membrane formation parameters and improving reproducibility compared to conventional manual casting methods [23]. This capability is particularly important for decoupling the effects of fabrication parameters on membrane structure and performance, which is difficult to achieve using conventional manual casting techniques.

Herein, we report a study with two main contributions. First, we systematically investigated the fabrication of advanced UF membranes by leveraging the precision of a commercially available, unmodified 3D printer. We elucidated the effects of casting temperature and casting speed on the morphology and performance of pristine PES membranes. Second, to develop a multifunctional membrane with superior antifouling and antibacterial capabilities, we incorporated our custom-synthesized, regenerable *N*-halamine polymer into the optimized membrane formulation. The resulting membranes were comprehensively characterized to establish clear structure–property-performance relationships, focusing on permeability, solute rejection, fouling resistance, mechanical stability, and biocidal efficacy.

Furthermore, to clarify the practical contribution of the proposed fabrication strategy, membranes produced via conventional manual casting were also prepared and compared with the 3D printer-assisted membranes in terms of permeability, selectivity, and structural properties. This comparative approach enables a more rigorous evaluation of the advantages provided by the 3D printer-assisted casting system and clearly demonstrates its benefits over conventional fabrication methods.

Materials and methods

Materials

The synthesis of *N*-(2-methyl-1-(4-methyl-2,5-dioxoimidazolidin-4-yl)propan-2-yl)acrylamide (HA) was conducted via a reaction involving *N*-(1,1-dimethyl-3-oxobutyl)acrylamide (DA; Aldrich), potassium cyanide (Merck), and ammonium carbonate (Sigma-Aldrich). Potassium persulfate (PPS; Acros) was used as the initiator in the polymerization process. Polyethersulfone (PES; Mw = 72,000 g mol^{-1}; Ultrason E6020P, BASF) was used to prepare the flat sheet membrane casting solutions. Polyvinylpyrrolidone (PVP, K30; Mw = 40,000 g mol^{-1}; P0472, TCI) was added as a pore-forming agent, while *N*-methyl-2-pyrrolidone (NMP; Acros) served as the solvent. Bovine serum albumin (BSA, Mw = 66,500 Da, Fisher Scientific, USA) was selected as a model protein foulant for all filtration and fouling experiments. Phosphate buffer solutions (PBS) were prepared from sodium dihydrogen phosphate dihydrate and disodium hydrogen phosphate (Merck, Germany) and were used to prepare and maintain the pH of the BSA solutions. All aqueous solutions were prepared using distilled water obtained from a GFL 2004 distillation system. All chemicals were used as received, without further purification.

Synthesis of hydantoin acrylamide monomer and poly(hydantoin acrylamide)

The synthesis of the HA monomer was performed via the Bucherer-Bergs reaction, adapting a procedure from Kocer et al. [24]. In a typical synthesis, the precursor N-(1,1-dimethyl-3-oxobutyl)acrylamide (DA, 17.093 g, 100 mmol) was reacted with potassium cyanide (13.565 g, 200 mmol) and ammonium carbonate (57.654 g, 600 mmol) in a 1:1 (v/v) ethanol/water mixture. The reaction was stirred at room temperature for 4 days. Upon completion, ethanol was removed by rotary evaporation, and the crude HA product was precipitated by acidifying the aqueous phase with dilute HCl. The resulting white solid was isolated by filtration and dried under vacuum.

Subsequently, the purified HA monomer was polymerized via free-radical polymerization. The monomer (2.0 g, 8.4 mmol) was dissolved in an aqueous solution, and potassium persulfate (PPS, 0.004 g) was added as the initiator. The polymerization was conducted at 75 °C for 5 h under a nitrogen atmosphere with continuous stirring. The final homopolymer (HP) was collected by filtration, and dried in a vacuum oven. The chemical structures of DA, HA, and HP are illustrated in Fig. 1.

Membrane fabrication

Preparation of the casting solutions

Homogeneous casting solutions were prepared by dissolving PES, PVP, and, where applicable, the custom-synthesized HP in NMP. The precise compositions for each membrane are detailed in Table 1. The mixtures were stirred at 23 ± 1 °C for 48 h to ensure complete

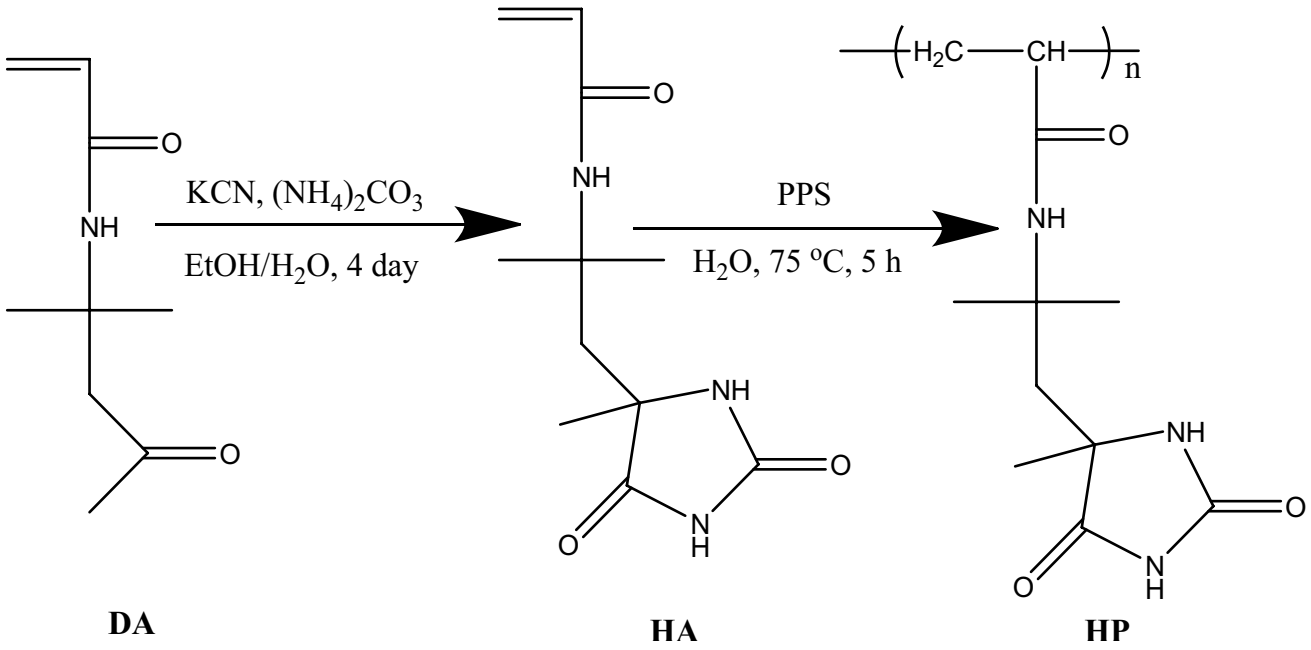


Figure 1 Chemical structure of DA, HA, and HP.

Table 1 Compositions and fabrication parameters of the UF membranes prepared via the 3D printer-assisted casting method

Membrane IDs	PES (wt%)	PVP (wt%)	HP (wt%)	NMP (wt%)	Casting Speed (mm s^{-1})	Casting Temperature (°C)	Chlorination
M0	18	3	–	79	**Not controlled**	**23**	–
M1	18	3	–	79	65	**30**	–
M2	18	3	–	79	65	**60**	–
M3	18	3	–	79	65	**90**	–
M4	18	3	–	79	**32.5**	60	–
M5	18	3	–	79	**97.5**	60	–
M6	18	3	–	79	**130**	60	–
M2-HP	**17.82**	3	**0.18**	79	65	60	–
M2*	18	3	–	79	65	60	+
M2-HP*	**17.82**	3	**0.18**	79	65	60	+

Membranes denoted by an asterisk (*) were subjected to a post-fabrication chlorination treatment

dissolution. One hour prior to casting, each solution was heated to its designated casting temperature to ensure thermal equilibrium.

Membrane fabrication via a 3D printing platform

UF membranes were fabricated using the non-solvent induced phase separation (NIPS) method. The membrane casting process was conducted using a 3D printer-assisted casting system, in which a commercial Elegoo Neptune 4 3D printer was employed as a precisely controlled motion and temperature platform rather than as a printing tool. The printer was operated in its stock, unmodified configuration, and its parameters including platform speed and temperature were precisely controlled through the manufacturer's open-source firmware (Klipper) and associated software, which enabled automated and remotely monitored operation. The casting procedure, illustrated schematically in Fig. 2, was as follows: The polymer solution, pre-heated using a hot plate (A), was poured onto a glass substrate (C) mounted on the printer's heated,

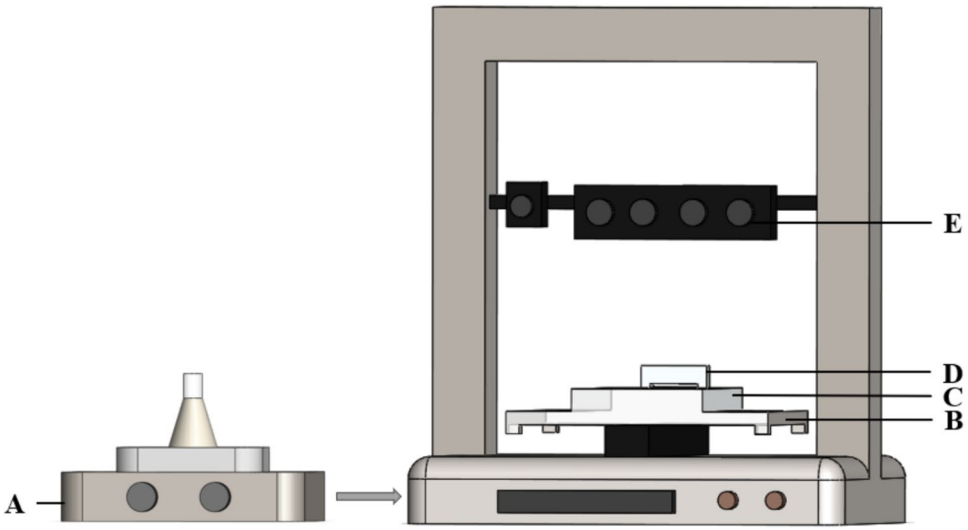


Figure 2 Schematic of the 3D printer-based membrane casting system, showing the main components: **A** hot plate, **B** heated X-axis movable plate, **C** glass substrate, **D** film applicator, and **E** Z-axis movable frame.

X-axis movable plate (B). A thin film with a nominal thickness of 200 μm was then cast by moving the platform at a preset speed under the film applicator (D), which was held stationary on the Z-axis movable frame (E). Immediately following casting, the nascent membrane was immersed in a coagulation bath of tap water (30 °C) and held for 48 h to complete the phase inversion process and solidify the final asymmetric porous structure.

Experimental design

A systematic study was conducted to elucidate the influence of the key fabrication parameters on the membrane properties, as summarized in Table 1.

Effect of Casting Temperature: To evaluate how casting temperature influences the process, a first set of membranes (M1, M2, and M3) was produced at a consistent platform speed of 65 mm s^{-1} (half of the printer's default speed), while the casting temperature was varied at 30, 60, and 90 °C.

Effect of Casting Speed: Based on the initial results, an optimal temperature of 60 °C was selected. A second set of membranes (M4, M5, and M6) was then prepared by modulating the platform speed to 32.5, 97.5, and 130 mm s^{-1} (corresponding to 25, 75, and 100% of the default 130 mm s^{-1} speed, respectively).

Effect of N-halamine Polymer (HP) Incorporation: Finally, to assess the impact of the functional additive, the *N*-halamine polymer was incorporated into the optimized formulation (based on membrane M2) to produce the M2-HP membrane. For comparative studies, a subset of membranes (M2 and M2-HP) was subjected to a post-fabrication chlorination treatment.

Control Membrane (M0): In addition to the 3D printer-assisted membranes, a control membrane (M0) was fabricated using a conventional manual casting method under ambient laboratory conditions. In this case, the casting speed was not precisely controlled and depended on operator handling. The cast film was immediately immersed in a coagulation bath at 30 °C to complete the phase inversion process. This membrane was prepared to provide a baseline for comparison in terms of permeability, thickness, and BSA rejection.

Membrane characterization and performance evaluation

Physicochemical and mechanical characterization

The chemical functionality of the membranes was analyzed by Fourier-transform infrared (FT-IR) spectroscopy using a Thermo Nicolet iS 50 spectrometer equipped with an attenuated total reflectance (ATR) accessory. Spectra were recorded from 4000 to 400 cm^{-1} at a resolution of 4 cm^{-1} over 32 scans.

The surface and cross-sectional morphologies were examined using a scanning electron microscope (SEM, Carl Zeiss Gemini 300). Prior to analysis, the samples were sputter-coated with a 15 nm Au–Pd layer. Images were acquired at an accelerating voltage of 10 kV under high-vacuum conditions (10^{-6} mbar).

The surface wettability was evaluated by static water contact angle measurements on a DataPhysics

OCA-15EC goniometer. The angle of a 4 μL deionized water droplet was recorded 10 s after deposition, and the reported values represent the average of at least three measurements taken at different locations on each membrane sample.

The membrane thickness was measured using a digital dial thickness gauge (Mitutoyo 543—790B-10) at five different points for each sample, and the reported value represents the average thickness.

The mechanical properties, namely tensile strength (TS) and elongation at break (EAB), were determined using a Shimadzu AGS-X universal testing machine. Specimens (10 mm × 60 mm) were tested at a crosshead speed of 10 mm min^{-1}, and the results were averaged from at least five measurements per membrane type.

The overall membrane porosity (ε) was determined gravimetrically using the wet/dry weight method [25, 26], given in Eq. (1):

$$\varepsilon = \left(\frac{W_w - W_d}{\rho_w \times A \times l}\right) \times 100 \quad (1)$$

where W_w and W_d are the weights of the wet and dry membranes (g), respectively, ρ_w is the density of pure water (0.998 g cm^{-3}), A is the total membrane area (cm^2), and l is the membrane thickness (cm). Subsequently, the mean pore radius (r_m) was calculated using the Guerout-Elford-Ferry (GEF) **Eq.** (2) incorporating the tortuosity factor [25–27]:

$$r_m = \sqrt{\frac{(2.9 - 1.75\varepsilon) \times 8\eta l J_w}{\varepsilon \times \Delta P}} \quad (2)$$

where η is the water viscosity (8.9×10^{-4} Pa·s), J_w is the pure water flux expressed in m s^{-1} (converted from L m^{-2} h^{-1}) and ΔP is the applied transmembrane pressure (100,000 Pa). The mean pore diameter was calculated as $2r_m$.

Chlorination, active chlorine quantification, and stability evaluation

The designated membranes were chlorinated by immersion in a commercial sodium hypochlorite solution (10%) for 60 min, with the pH adjusted to 7 using 6 N HCl. After thorough rinsing, the membranes were dried at 37 °C for 3 h. The active chlorine content (Cl^+, wt%) loaded onto the membranes was quantified by iodometric/thiosulfate titration and calculated using Eq. (3):

$$Cl^+\% = \left(\frac{35.45 \times N \times V}{2 \times W}\right) \times 100 \quad (3)$$

where N is the normality of the sodium thiosulfate solution, V is the titrant volume (mL), and W is the sample weight (g).

To evaluate the long-term stability of the incorporated HP polymer and potential leaching of *N*-halamine functionalities, the membranes were immersed in distilled water at room temperature for 6 months. After this period, the membranes were re-chlorinated and the active chlorine content was quantified by iodometric titration.

Filtration performance

All filtration tests were performed at a constant transmembrane pressure of 1 bar using a dead-end stirred cell (HP4750, Sterlitech) with an effective membrane area of 14.6 cm^2. The membranes were pre-conditioned by immersion in distilled water for seven days.

Permeability and Rejection The pure water flux (PWF) was determined by filtering the deionized water and calculated using Eq. (4).

$$J_w = \frac{V}{A \times t} \quad (4)$$

where V is the volume of permeated water (L), A is the effective membrane area (0.00146 m^2), and t is the permeation time (h).

Bovine serum albumin (BSA) rejection was tested using a 1 g L^{-1} BSA solution (0.1 M phosphate buffer, pH 7). The feed (c_f) and permeate (c_p) concentrations were measured via UV–Vis spectrophotometry at 280 nm, and the rejection (R, %) was calculated using **Eq.** (5)**.** All reported values are an average of three independent tests.

$$R(\%) = \left(\frac{c_f - c_p}{c_f}\right) \times 100 \quad (5)$$

Antifouling Properties Fouling resistance was evaluated in a cyclic manner. An initial pure water flux (J_{w1}) was recorded, followed by a 1 h filtration of the BSA solution. The membrane was then physically cleaned by backwashing (BW) with water for 60 min. This fouling-cleaning cycle was repeated. Subsequently, a chemical wash (CW) was performed by immersing the fouled membrane in the sodium hypochlorite solution for 60 min. The flux recovery

ratio (FRR, %), indicating the cleaning efficiency, was calculated using **Eq.** (6), where J_{w2} is the pure water flux after cleaning. FRR reflects the cleaning efficiency and the extent of reversible fouling.

$$FRR(\%) = \left(\frac{J_{w2}}{J_{w1}}\right) \times 100 \quad (6)$$

Antibacterial activity

The biocidal activity of the membranes was evaluated according to the ASTM E2149 standard against both *Staphylococcus aureus* (ATCC 6538) and *Escherichia coli* (ATCC 35218). Membrane samples (0.5 g) were incubated in 50 mL of a bacterial suspension (~ 5.6×10^5 CFU mL^{-1}) under constant shaking. Aliquots were withdrawn after 15 and 30 min, serially diluted in phosphate-buffered saline (PBS), and plated on Mueller–Hinton II agar. After 24 h of incubation at 37 °C, the viable colonies were counted, and the efficacy was expressed as the log reduction in bacterial concentration.

Results and discussion

Confirmation of the *N*-halamine polymer incorporation and chlorination

To verify the successful incorporation of the HP polymer and its subsequent activation via chlorination, the membranes were analyzed by FT-IR spectroscopy and iodometric titration. As shown in Fig. 3, the spectrum of the unmodified M2 membrane was compared with those of the modified membranes. The M2-HP spectrum exhibited new, characteristic absorption bands at 1731 and 1776 cm^{-1}, which are

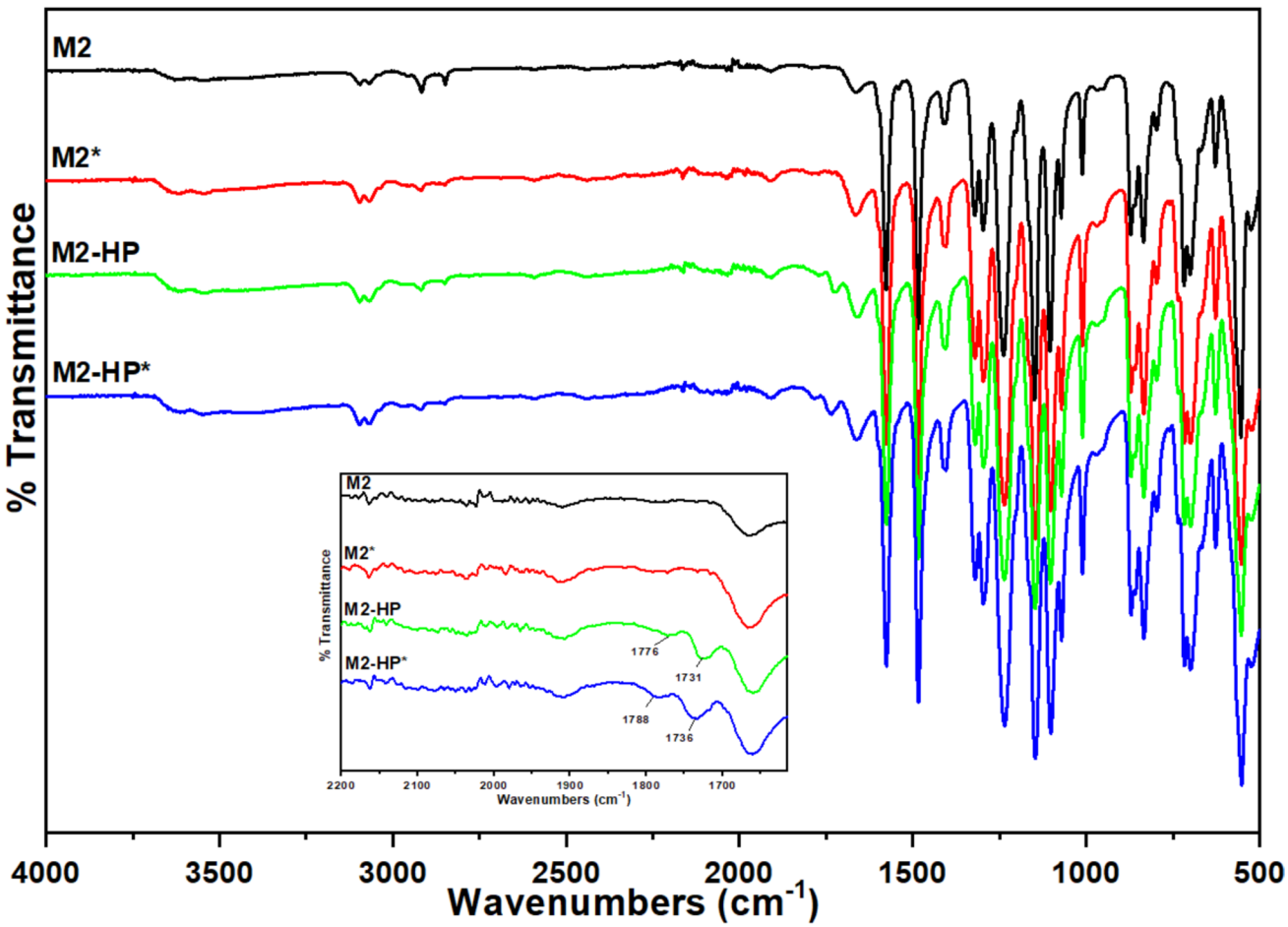


Figure 3 Comparative FT-IR spectra of the M2, M2*, M2-HP, and M2-HP* membranes.

assigned to the carbonyl stretching vibrations of the amide and imide moieties within the HP polymer, respectively [28]. The presence of these bands confirms the successful integration of the HP polymer into the PES membrane matrix.

Upon chlorination, these characteristic bands shifted to higher wavenumbers, appearing at 1736 and 1788 cm^{-1}, respectively [15]. This shift is consistent with the conversion of N–H groups to N-Cl bonds and thus confirms the formation of *N*-halamine moieties within the M2-HP* membrane. These spectral changes provide strong evidence for the structural transformation responsible for the biocidal potential of the membrane.

These spectroscopic findings were quantitatively corroborated by the titration results. As expected, the pristine (M2), chlorinated pristine (M2*), and unchlorinated modified (M2-HP) membranes did not exhibit active chlorine content (0%). In stark contrast, the chlorinated M2-HP* membrane exhibited a significant Cl^+ content of 0.31 wt% [15]. Taken together, the spectroscopic evidence of N-Cl bond formation and the quantitative measurement of active chlorine provide strong evidence of the successful *N*-halamine functionalization and activation of the M2-HP* membrane, establishing the chemical basis for its biocidal functionality.

The long-term stability test further demonstrated the exceptional durability of the HP polymer within the PES matrix. After 6 months of continuous immersion in distilled water, the M2-HP membrane retained an active chlorine content of approximately 0.28 wt% upon re-chlorination. This minimal decrease confirms that the HP polymer is stably immobilized within the membrane matrix without significant leaching, thus ensuring long-term, regenerable biocidal efficacy.

Optimization of the pristine membrane fabrication

The performance of the pristine membranes was systematically evaluated to identify the optimal fabrication parameters, and the results are summarized in Table 2**.** The investigation focused on the effects of casting method (manual vs. automated), casting temperature, and casting speed on PWF, BSA rejection, and membrane thickness.

To assess the contribution of the 3D printer-assisted casting system, the manually cast control membrane (M0) was first compared with the automated membranes. As shown in Table 2, M0 exhibited a relatively high variability in pure water flux (137 ± 44 L m^{-2} h^{-1}) along with greater thickness (145.0 ± 2.6 μm), indicating less uniform membrane formation. This behaviour can be attributed to variations in shear conditions and manual handling during casting. In contrast, the 3D printer-assisted membranes (e.g., M1, M2) showed improved reproducibility and more consistent structural properties, owing to the controlled and stable casting conditions.

Following this, the influence of casting temperature was evaluated (M1, M2, and M3) at a constant casting speed of 65 mm s^{-1}. The PWF reached a maximum value of 239 ± 29 L m^{-2} h^{-1} for the membrane cast at 60 °C (M2). At a lower temperature (30 °C, M1), the flux decreased, while at a higher temperature (90 °C, M3), a significant reduction in permeability was observed (98 ± 33 L m^{-2} h^{-1}). Notably, M3 exhibited the lowest thickness (90.6 ± 0.8 μm) but also the lowest flux. This can be explained by accelerated solvent evaporation at elevated temperatures, leading to the formation of a denser top layer and reduced effective pore size, thereby increasing hydraulic resistance [29, 30]. Despite these changes, BSA rejection remained consistently high (> 90%) across all temperatures.

Table 2 Pure water flux (PWF), BSA rejection, and average thickness of the control (M0) and pristine 3D printer-assisted membranes (M1-M6) fabricated under various casting conditions

Membrane IDs	PWF (L m^{-2} h^{-1})	BSA rejection (%)	Membrane thickness (μm)
M0 (manual)	137 ± 44	90.9 ± 0.7	145.0 ± 2.6
M1 (30 °C, 3D-assisted)	192 ± 26	90.3 ± 0.7	139.4 ± 0.5
M2 (60 °C, 3D-assisted)	239 ± 29	91.1 ± 0.7	123.2 ± 0.8
M3 (90 °C, 3D-assisted)	98 ± 33	90.8 ± 0.7	90.6 ± 0.8
M4 (32.5 mm s^{-1}, 3D-assisted)	229 ± 29	92.7 ± 2.1	125.2 ± 0.8
M5 (97.5 mm s^{-1}, 3D-assisted)	165 ± 10	97.0 ± 0.7	120.6 ± 1.0
M6 (130 mm s^{-1}, 3D-assisted)	208 ± 29	96.7 ± 0.4	119.0 ± 1.3

At the optimized temperature (60 °C), the effect of casting speed was further investigated (M4, M2, M5, and M6). The membrane thickness remained relatively stable, indicating that casting speed had a limited effect on the overall morphology. While all membranes exhibited high BSA rejection (> 92%), the M2 membrane (65 mm s^{-1}) provided the highest PWF. Higher casting speeds (e.g., M5 and M6) slightly increased rejection but resulted in a moderate decrease in permeability, possibly due to the formation of a more compact surface structure.

Overall, the M2 membrane (60 °C, 65 mm s^{-1}) exhibited the best balance between permeability, selectivity, and structural consistency, and was therefore selected as the optimal condition for subsequent incorporation of the *N*-halamine polymer.

Evaluation of the fouling resistance and flux recovery

A clear advantage of incorporating the HP polymer was demonstrated through a comprehensive fouling and cleaning study, comparing the optimized M2 with its modified counterpart M2-HP. The time-dependent flux profiles shown in Fig. 4a illustrate the fouling and cleaning behaviour of both membranes when subjected to BSA filtration, followed by back-washing (BW) and chemical-washing (CW) cycles.

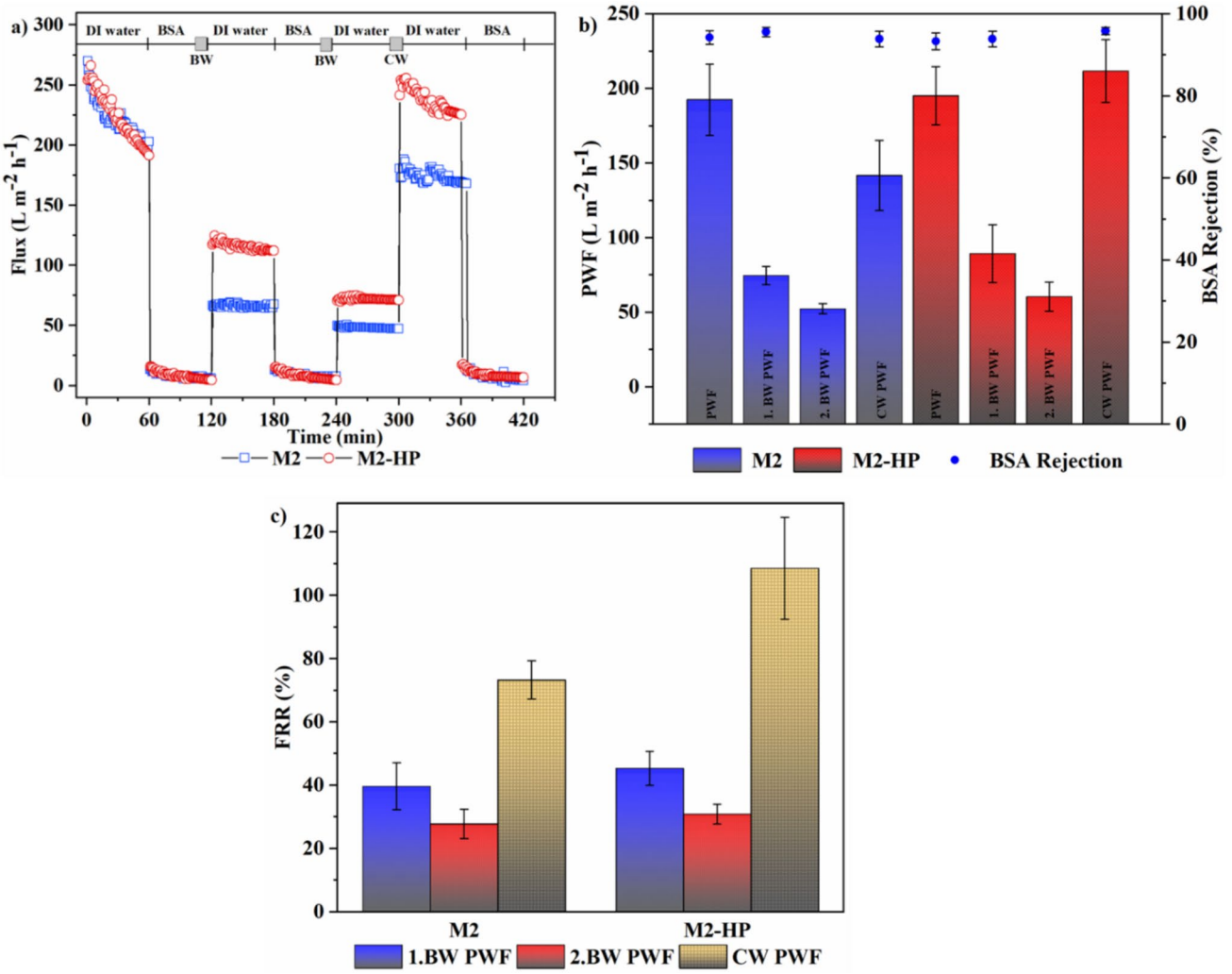


Figure 4 Antifouling and cleaning performance of the M2 and M2-HP membranes: **a** time-dependent flux profiles during the fouling and cleaning cycles; **b** stepwise comparison of the pure water flux (PWF) at different stages; and c final flux recovery ratios (FRR) after cleaning.

While both membranes exhibited a sharp flux decline upon exposure to BSA, the M2-HP membrane consistently maintained a higher flux throughout the fouling and physical cleaning stages. The bar charts in Fig. 4b quantify this behaviour, showing the stepwise recovery after each cleaning procedure. However, a clear indication of the modification's effect is revealed in the FRR after CW, as shown in Fig. 4c.

Following CW with sodium hypochlorite, the M2 membrane's flux recovered to only 73.2% of its initial value, indicating significant irreversible fouling. In contrast, the M2-HP membrane exhibited a significantly higher FRR of 108.6%, indicating that its permeability was not only restored but also exceeded its original, pre-fouled state [31].

It should be noted that FRR values exceeding 100% may be attributed to physicochemical changes induced during sodium hypochlorite cleaning, such as the removal of residual foulants or pore-blocking species. In membrane systems, post-treatment or cleaning steps are known to improve pore accessibility by removing such residual species [32, 33]. Since the membranes in this study were used without any prior post-treatment, the chemical cleaning step may have contributed to an apparent increase in flux, which may partially explain the observed FRR values exceeding 100%. However, the consistently high BSA rejection (> 95%, Fig. 4b) observed after cleaning confirms that membrane selectivity was preserved, indicating that no significant pore enlargement or structural degradation occurred. This behaviour is attributed to the dual effect of hypochlorite treatment, which removes the protein foulant layer while simultaneously regenerating the *N*-halamine moieties on the membrane surface [34, 35]. This combined effect enhances cleaning efficiency and contributes to the observed high flux recovery.

This finding suggests that the incorporation of the HP polymer endows the membrane with enhanced and regenerable antifouling properties, making it suitable for long-term applications requiring periodic chemical cleaning.

Membrane morphology

The morphology of the fabricated membranes was investigated by SEM to establish a structural basis for their filtration performance (Fig. 5). All pristine membranes (M1-M6) exhibited the characteristic asymmetric architecture of UF membranes prepared via phase inversion, consisting of a dense, selective top layer supported by a porous substructure with well-defined finger-like macrovoids [36].

The casting temperature was found to have a significant impact on this morphology. Although the membrane cast at 90 °C (M3) was the thinnest of the series, it paradoxically delivered the lowest water flux. This discrepancy is explained by accelerated solvent evaporation due to high casting temperature, which created a dense, polymer-rich skin on the film surface prior to coagulation. This skin layer subsequently restricted the formation of an open, porous substructure, resulting in a morphology with high hydraulic resistance. This restrictive structure, not the membrane's thickness, was a major factor influencing its permeability [37]. The M2 membrane (60 °C), in contrast, offered the best compromise between a well-balanced morphology and high performance. In contrast to temperature, variations in casting speed (membranes M4, M5, and M6) did not induce significant changes in the cross-sectional morphology, indicating that this parameter had a less dominant influence on the final structure.

To further elucidate the effect of *N*-halamine functionalization on membrane structure and fouling behaviour, SEM analyses were conducted before and after filtration experiments (Fig. 6 and 7).

As shown in Fig. 6, all membranes (M2, M2*, M2-HP, and M2-HP*) exhibited very similar surface and cross-sectional morphologies prior to filtration. The top surfaces appeared relatively smooth and dense, while the cross-sections revealed the typical asymmetric structure with a thin selective layer supported by a porous substructure. No significant differences in pore distribution or structural integrity were observed among the membranes, indicating that neither *N*-halamine incorporation nor chlorination altered the fundamental membrane architecture. This observation is consistent with the comparable porosity and mean pore diameter values obtained from the GEF analysis.

After filtration, fouling, and cleaning processes (Fig. 7), no significant differences were observed in the overall surface morphology between the M2 and M2-HP membranes. Both membranes exhibited comparable surface features, indicating that the fouling and subsequent cleaning processes did not lead to noticeable structural alterations. It is well known that the incorporation of additives into membrane formulations can disrupt the pore structure and often adversely affect permeability or rejection [19, 38].

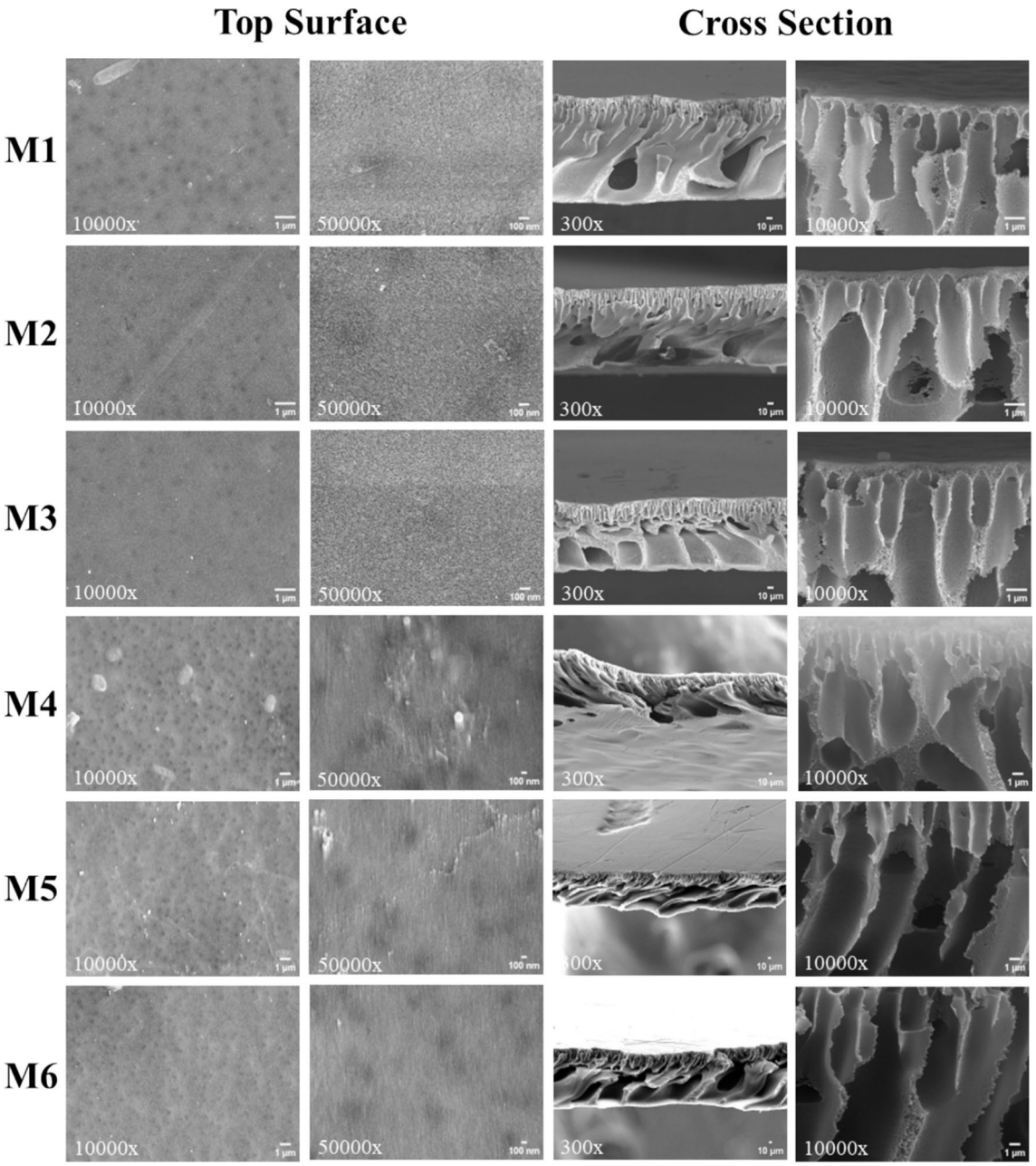


Figure 5 SEM micrographs showing the top surface (10,000 ×, 50,000 ×) and cross-sectional (300 ×, 10,000 ×) morphologies of the pristine membranes (M1-M6).

However, in this study, the use of a very low HP loading (0.18 wt%) allowed the membrane structure to be preserved. Furthermore, even after chemical cleaning with sodium hypochlorite solution (10%, pH 7), no evident pore collapse, enlargement, or structural damage was observed [39, 40].

Overall, these results confirm that both the incorporation of the *N*-halamine polymer and the applied cleaning conditions did not compromise the membrane's porous architecture. Therefore, the observed improvements in antifouling performance can be attributed primarily to surface chemical effects rather than changes in bulk membrane structure.

To quantitatively evaluate the membrane structure, the overall porosity was determined using the wet/dry gravimetric method, while the mean pore diameter

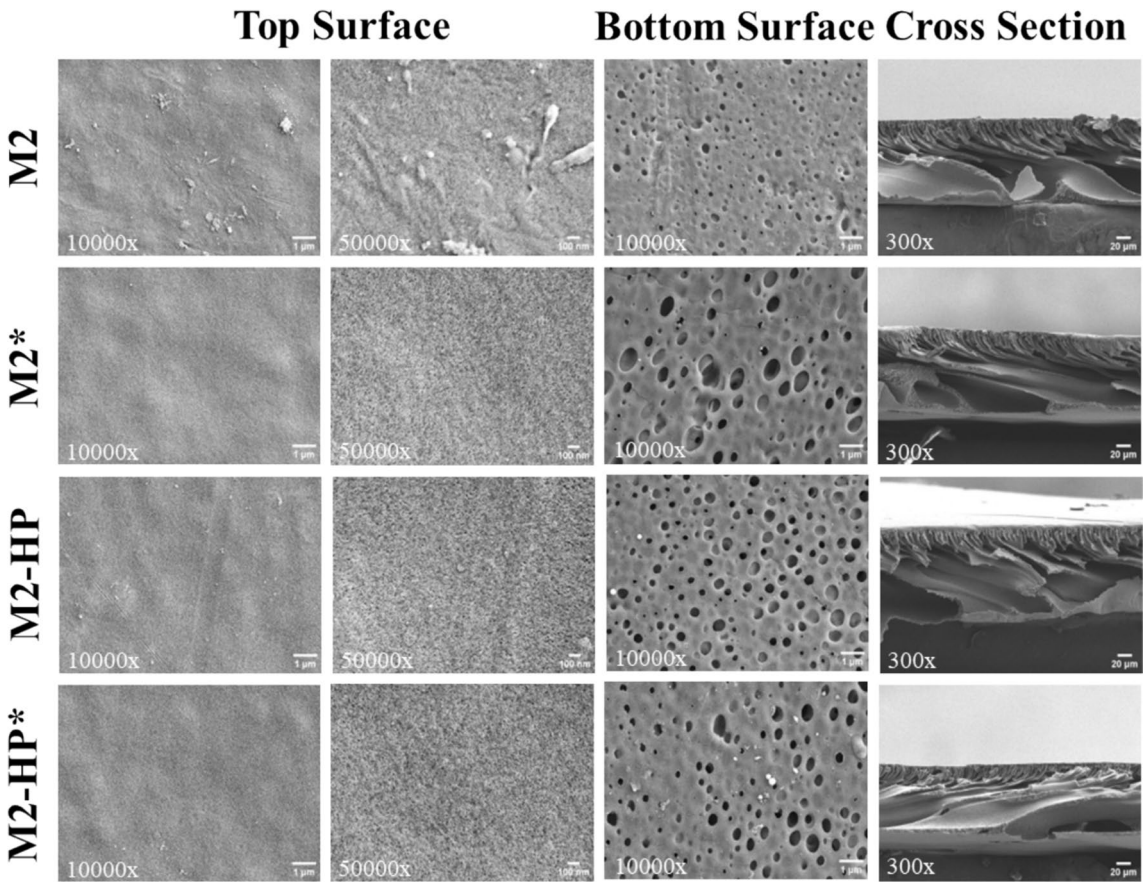


Figure 6 SEM images of the top surface (10,000 ×, 50,000 ×), bottom surface (10,000 ×), and cross-sectional morphology (300 ×) of M2, M2*, M2-HP, and M2-HP* membranes.

was estimated using the GEF equation. Prior to weighing, the wet membranes were gently placed between absorbent tissues and subjected to a constant load (600 g) to remove excess surface water, ensuring consistent and reproducible measurements of the retained water within the membrane pores. The porosity values were then calculated based on the volume fraction of water within the membrane matrix, providing an indication of the total void fraction.

The mean pore diameter values obtained from the GEF model represent effective average pore sizes derived from hydraulic permeability data, assuming simplified conditions such as cylindrical pores, uniform pore distribution, and complete pore connectivity [41]. As summarized in Table 3, the membranes exhibited porosity values in the range of 67.2 ± 2.7% to 75.9 ± 2.7% and mean pore diameters between 60.1 ± 9.7 and 70.3 ± 5.6 nm, which are consistent with typical ultrafiltration membranes reported in the literature [27].

Importantly, no significant differences were observed between pristine, modified, and chlorinated membranes, indicating that neither the incorporation of the *N*-halamine polymer nor the subsequent chemical treatment altered the intrinsic porous structure. It should be emphasized that the pore size values calculated using the GEF equation are theoretical estimations and may not directly correspond to visible pore features in SEM images [42]. This is particularly relevant for ultrafiltration membranes, where the dense selective skin layer dominates the surface morphology [43].

Consistent with this, the SEM results (Fig. 6 and 7) showed no noticeable differences in surface or cross-sectional morphology among the membranes, further confirming that the structural integrity was preserved. Therefore, the observed differences in filtration and antifouling performance can be attributed primarily to surface chemical modifications rather than changes in pore structure.

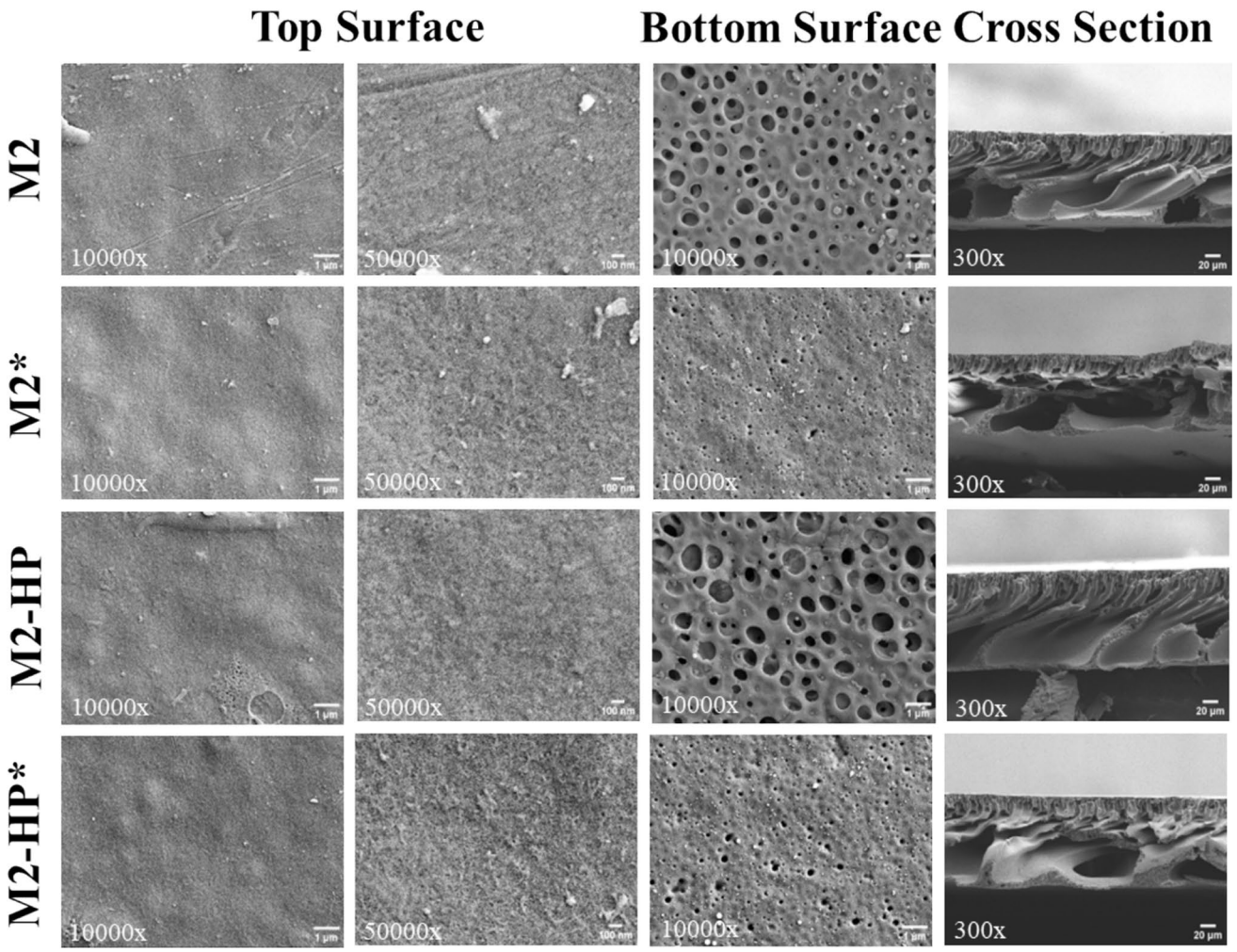


Figure 7 SEM images of the top surface (10,000 ×, 50,000 ×), bottom surface (10,000 ×), and cross-sectional morphology (300 ×) of M2, M2*, M2-HP, and M2-HP* membranes after filtration, BSA fouling, backwashing, chemical washing, and subsequent flux measurement.

Surface wettability

The surface wettability, a critical factor for permeability and fouling resistance, was evaluated via contact angle measurements (Fig. 8). The results revealed a complex relationship between surface chemistry and the underlying physical structure. For instance, while the enhanced hydrophilicity of the M2 membrane compared to M1 was consistent with its higher water flux, a more complex relationship was observed for the membrane cast at 90 °C (M3). Although the M3 membrane was the most hydrophilic in this series (Fig. 8a), it paradoxically delivered the lowest water flux. As discussed in the morphological analysis (Sect. "Membrane morphology"), this discrepancy is explained by accelerated solvent evaporation at high temperatures. The resulting dense, polymer-rich skin restricted the formation of an open porous substructure, leading to a morphology with high hydraulic resistance. These findings indicate that membrane performance is governed by a combination of structural and surface-related factors, rather than wettability alone [44, 45].

Table 3 Porosity and mean pore diameter of pristine, modified, and chlorinated membranes estimated using the guerout–elford–ferry (GEF) equation

Membrane ID	Porosity (%)	Mean pore diameter (nm)
M2	74.9 ± 4.1	60.1 ± 9.7
M2*	67.2 ± 2.7	70.3 ± 5.6
M2-HP	75.9 ± 2.7	62.3 ± 4.3
M2-HP*	73.9 ± 3.5	66.2 ± 6.8

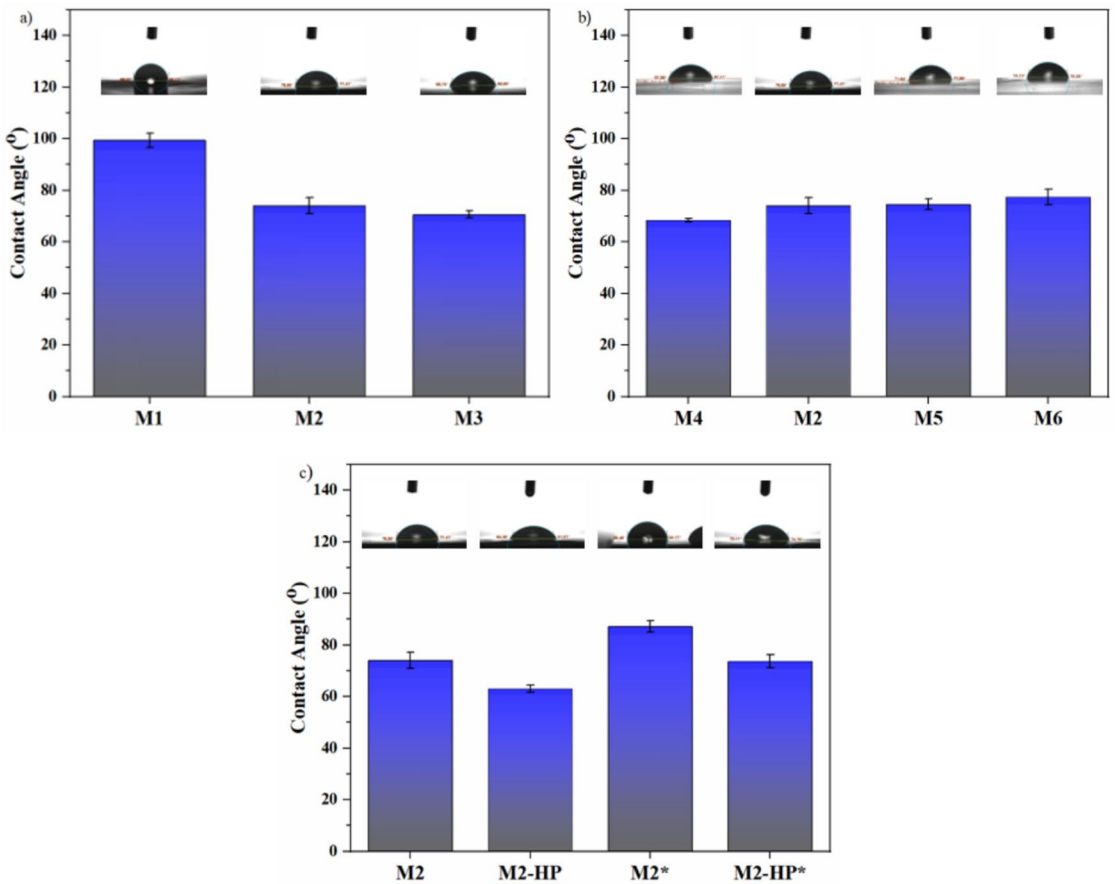


Figure 8 Contact angle measurements showing the effect of **a** casting temperature, **b** casting speed, and **c** *N*-halamine modification and chlorination.

The effect of casting speed showed a different trend (Fig. 8b). An increase in the casting speed from 32.5 (M4) to 130 mm s^{-1} (M6) resulted in a slight increase in the contact angle, from 68.8° to 77.4°. This indicates that the membranes prepared at higher speeds had a slightly more hydrophobic surface. This observation is consistent with the permeability results (Table 2), where the higher-speed membranes (M5, M6) also showed lower water flux compared to M2 and M4.

The incorporation of the HP polymer, however, provided a direct and beneficial enhancement of the surface properties. As demonstrated in Fig. 8c, the addition of HP caused a substantial decrease in the contact angle from 74 (M2) to 63° (M2-HP), confirming the creation of a more hydrophilic surface. This modification is likely to contribute to the membrane's improved antifouling performance by mitigating the initial adsorption of protein foulants.

Interestingly, the chlorination treatment consistently increased the contact angle for both the M2* and M2-HP* membranes, indicating a slight increase in the surface hydrophobicity. While the conversion of N–H to the less polar N-Cl bonds in the M2-HP* membrane likely contributes to this effect, the fact that the M2* membrane also became more hydrophobic suggests that other factors, such as interactions between chlorine and the PES/PVP backbone, may also be involved [15].

In conclusion, the interplay between morphology and surface chemistry dictates the final membrane performance. In addition, the contact angle results are broadly consistent with the porosity and pore size data presented in Table 3. While the incorporation of HP did not significantly alter the membrane porosity or pore size, indicating that the observed improvement in wettability is mainly attributed to surface chemistry, the slight changes observed after chlorination suggest that variations in porosity and pore structure may also contribute to the measured contact angle values. While a hydrophilic surface

can be beneficial for high flux and fouling resistance, its effect may be limited by a restrictive physical structure [46]. The improved performance of the M2-HP membrane may therefore be attributed to the combination of enhanced surface hydrophilicity and preservation of the porous architecture.

Mechanical properties of the membrane

The mechanical properties of the membranes were evaluated to assess their suitability for practical applications (Fig. 9). As shown in Fig. 9a, the casting temperature significantly influenced the mechanical robustness. An increase in temperature from 30 (M1) to 90 °C (M3) led to a gradual improvement in both tensile strength and elongation at break. This trend is directly consistent with the morphological changes driven by accelerated solvent evaporation at higher temperatures [47]. As discussed previously, the rapid evaporation at 90 °C promoted the formation of a denser, more compact, and sponge-like polymer matrix. This less porous and more integrated structure is responsible for the observed enhancement in mechanical properties. In contrast, the effect of casting speed was less pronounced, with no clear trend observed for either tensile strength or elongation (Fig. 9b).

A key finding is presented in Fig. 9c, which compares the M2 membrane with its modified and chlorinated counterparts. The results unequivocally show that the incorporation of the HP polymer and the subsequent chlorination steps had no significant adverse effect on the membrane's mechanical integrity. This preservation of mechanical robustness is a

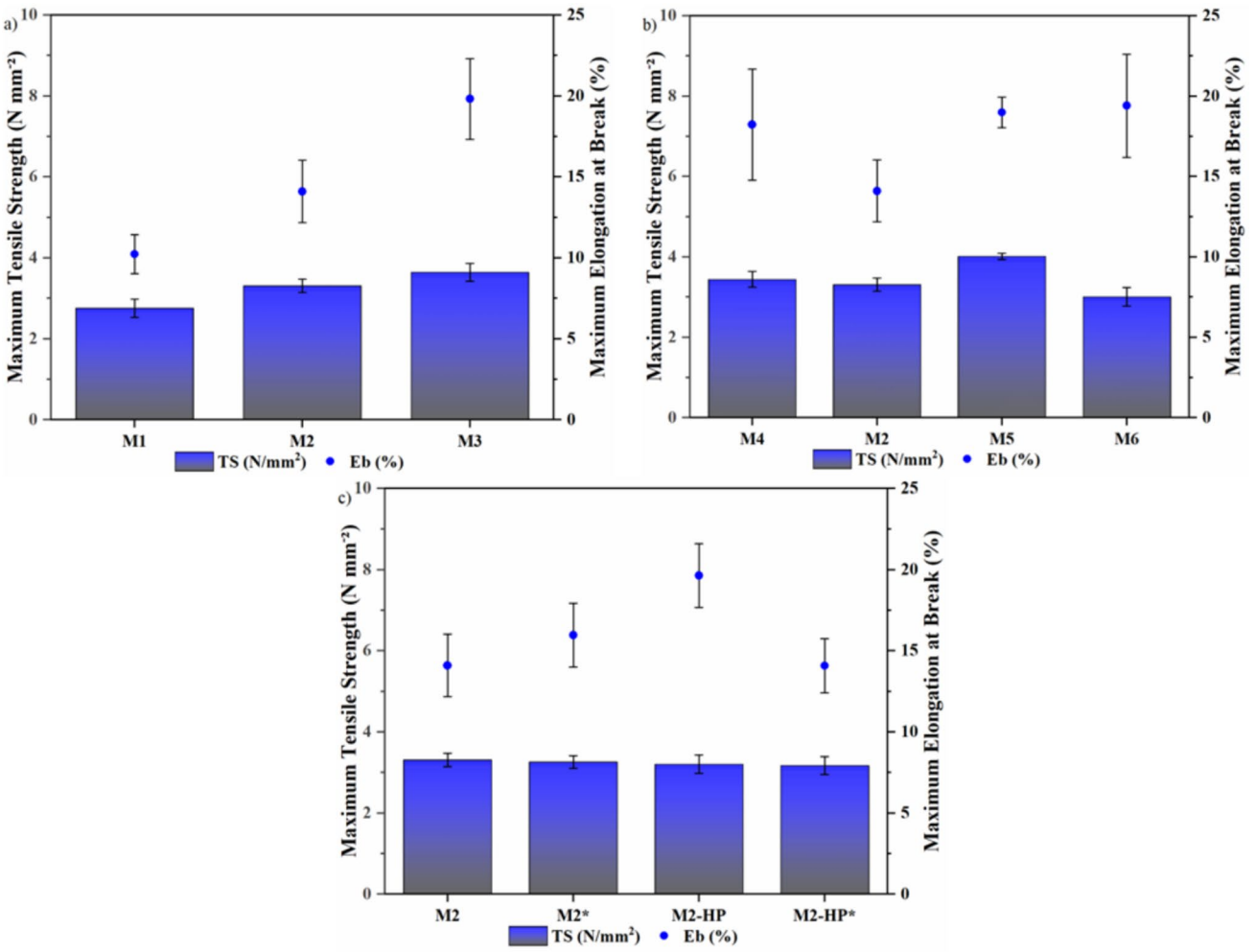


Figure 9 Mechanical properties of the membranes showing the effect of **a** casting temperature, **b** casting speed, and **c** *N*-halamine modification and chlorination.

critical finding, as it confirms that the powerful antifouling and antibacterial functionalities were successfully imparted without a trade-off in mechanical stability. This ability to create a high-performance, multifunctional membrane that retains the inherent robustness of the parent polymer validates the practical viability of this *N*-halamine modification strategy for developing durable, long-lasting membrane systems.

Assessment of antibacterial activity

The final and critical performance advantage of *N*-halamine functionalization is the potent biocidal activity imparted to the membrane. The antibacterial efficacy was evaluated against both Gram-positive (*S. aureus*) and Gram-negative *(E. coli*) bacteria, with the results summarized in Table 4. In addition, Fig. 10 presents the visual representation of the antibacterial results after 15 min of contact, corresponding to the numerical data given in Table 4, with Fig. 10a showing *Staphylococcus aureus* and Fig. 10b showing *Escherichia coli*.

As shown in the table, M2, chlorinated M2*, and M2-HP membranes exhibited negligible antibacterial efficacy. Although a slight reduction in bacteria was observed for these samples, this minor effect is attributed to the physical entrapment of some cells within the porous membrane structure rather than any true biocidal action. This distinction is a crucial finding, as it definitively demonstrates that neither chlorination alone nor the mere presence of the HP polymer is sufficient to induce significant biocidal activity.

In stark contrast, the chlorinated M2-HP* membrane demonstrated an extremely rapid and effective biocidal action. Within just 15 min of contact, it achieved a complete kill (> 5.7-log reduction) of both *S. aureus* and *E. coli*. This rapid and broad-spectrum inactivation highlights the synergistic effect of combining the HP polymer with a chlorination treatment,

Table 4 Antibacterial activity of the pristine and modified membranes against *S. aureus* and *E. coli* after 15 and 30 min of contact

Membrane samples	Antibacterial efficacy of the membranes							
	15 min				30 min			
	S. aureus		*E. coli*		*S. aureus*		*E. coli*	
	(%)	log	(%)	log	(%)	log	(%)	log
M2	− 11.29	− 0.05	− 0.13	0.00	− 29.03	− 0.15	− 3.28	− 0.01
M2*	− 20.81	− 0.10	− 49.43	− 0.30	− 25.81	− 0.13	− 51.37	− 0.31
M2-HP	− 22.58	− 0.11	− 74.25	− 0.59	− 27.42	− 0.14	− 81.23	− 0.73
M2-HP*	− 100.00	− 5.75	− 100.00	− 5.74	− 100.00	− 5.75	− 100.00	− 5.74

The initial bacterial concentrations were approximately 5.6×10^5 CFU mL^{-1} (log 5.75) for *S. aureus* and 5.5×10^5 CFU mL^{-1} (log 5.74) for *E. coli.* Positive (+) and negative (-) signs indicate an increase and a reduction in viable counts, respectively

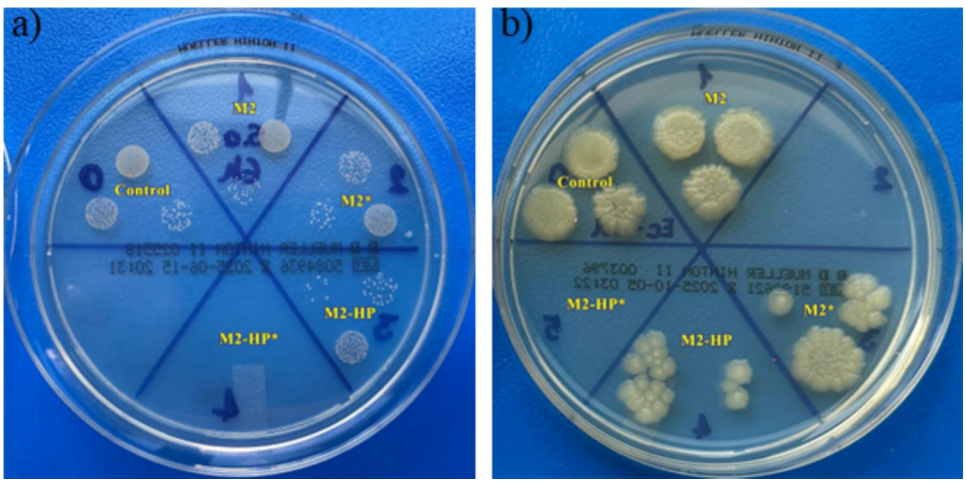


Figure 10 Visual representation of antibacterial activity after 15 min of contact: **a** *Staphylococcus aureus* and **b** *Escherichia coli*.

which activates the *N*-halamine moieties, as confirmed by our spectroscopic and titration data [48].

The ability to achieve such a high level of disinfection in a very short contact time significantly broadens the application potential of these membranes. In fields such as water purification and biomedical devices, the capacity to rapidly inactivate pathogens is paramount for preventing the initial stages of bacterial adhesion and subsequent biofilm formation. Therefore, these findings establish the functionalized membrane as a promising platform for applications where both high-performance separation and robust, on-demand antibacterial protection are required.

Conclusions

This study successfully demonstrated the fabrication of high-performance, multifunctional ultrafiltration membranes by combining a novel manufacturing approach with advanced polymer chemistry. We have shown that a 3D printer-assisted casting system, employing a commercial, unmodified 3D printer as a precisely controlled motion and temperature platform, can be effectively utilized for the accurate and reproducible fabrication of ultrafiltration membranes. This approach represents a simple, low-cost, and open-source alternative to conventional laboratory-scale casting setups while maintaining full compatibility with the non-solvent induced phase separation (NIPS) process.

The key innovation of this work was the incorporation of a custom-synthesized HP into an optimized PES membrane matrix. This modification proved to be highly effective: the *N*-halamine-modified membrane exhibited superior and regenerable antifouling performance, achieving a high flux recovery ratio (~ 109%) after chemical washing significantly surpassing that of the unmodified control (~ 73%). This indicates that the membrane's performance can be not only fully restored but also enhanced through chemical washing, a crucial attribute for long-term operational stability. Furthermore, the chlorinated *N*-halamine-modified membrane demonstrated potent and rapid antibacterial activity, achieving a > 5-log reduction of both *S. aureus* and *E. coli* within only 15 min of contact. In addition, porosity and mean pore size analyses confirmed that the structural properties of the membranes were preserved after modification and chemical cleaning. Long-term stability tests further demonstrated that the active chlorine content remained largely unchanged after 6 months, indicating stable immobilization of the *N*-halamine polymer within the membrane matrix.

Crucially, these substantial performance enhancements were achieved without adversely affecting the membrane's intrinsic porous architecture or its mechanical integrity. By creating a membrane that is simultaneously high-performing, robust, regenerable, and rapidly antibacterial, this work paves the way for the development of advanced materials for a wide range of critical applications, including water purification, food and beverage processing, and biomedical devices.

Acknowledgements

This study was financially supported by the Bursa Technical University Scientific Research Projects (BAP) Coordination Unit under project number 240D012.

Author contributions

Ahmet Aydın, Methodology, Investigation, Visualization, Writing-Original Draft, Fatma Demirci, Investigation, Visualization, Writing-Original Draft, Mehmet Orhan, Investigation, Validation, Writing-Review & Editing, Hasan Basri Koçer, Supervision, Project Administration, Funding Acquisition, Resources, Writing-Review & Editing.

Funding

Open access funding provided by the Scientific and Technological Research Council of Türkiye (TÜBİTAK).

Data availability

The datasets generated during and/or analysed during the current study are available from the corresponding author on reasonable request.

Declarations

Conflict of interest The authors declare that they have no known competing financial interests or personal relationships that could potentially influence the work reported in this paper.

Open Access This article is licensed under a Creative Commons Attribution 4.0 International License, which permits use, sharing, adaptation, distribution and reproduction in any medium or format, as long as you give appropriate credit to the original author(s) and the source, provide a link to the Creative Commons licence, and indicate if changes were made. The images or other third party material in this article are included in the article's Creative Commons licence, unless indicated otherwise in a credit line to the material. If material is not included in the article's Creative Commons licence and your intended use is not permitted by statutory regulation or exceeds the permitted use, you will need to obtain permission directly from the copyright holder. To view a copy of this licence, visit http://creativecommons.org/licenses/by/4.0/.

References

[1] Baker RW (2023) Membrane technology and applications. Wiley, New York

[2] Mulder M (1991) Basic principles of membrane technology. Springer, New York

[3] Ulbricht M (2006) Advanced functional polymer membranes. Polymer (Guildf) 47:2217–2262. https://doi.org/10.1016/j.polymer.2006.01.084

[4] Loeb S, Sourirajan S (1963) Sea water demineralization by means of an osmotic membrane. ACS Publications, pp 117–132

[5] Bohn PW, Elimelech M, Georgiadis JG et al (2009) Science and technology for water purification in the coming decades. Nanosci Technol A Collect Rev Nat J 452:337–346. https://doi.org/10.1142/9789814287005_0035

[6] Chew JW, Kilduff J, Belfort G (2020) The behavior of suspensions and macromolecular solutions in crossflow microfiltration: an update. J Memb Sci 601:1–58. https://doi.org/10.1016/j.memsci.2020.117865

[7] Le-Clech P, Chen V, Fane TAG (2006) Fouling in membrane bioreactors used in wastewater treatment. J Memb Sci 284:17–53. https://doi.org/10.1016/j.memsci.2006.08.019

[8] Nunes SP, Peinemann K-V (2006) Membrane technology: in the chemical industry. Wiley, New York

[9] Upadhyaya L, Semsarilar M, Deratani A, Quemener D (2017) Nanocomposite membranes with magnesium, titanium, iron and silver nanoparticles-a review. J Membr Sci Res 3:187–198

[10] Olimattel K, Church J, Lee WH et al (2020) Enhanced fouling resistance and antimicrobial property of ultrafiltration membranes via polyelectrolyte-assisted silver phosphate nanoparticle immobilization. Membranes (Basel) 10:1–17. https://doi.org/10.3390/membranes10100293

[11] Kenawy ER, Worley SD, Broughton R (2007) The chemistry and applications of antimicrobial polymers: a state-of-the-art review. Biomacromol 8:1359–1384. https://doi.org/10.1021/bm061150q

[12] Yu H, Zhang X, Zhang Y et al (2013) Development of a hydrophilic PES ultrafiltration membrane containing SiO2@N-Halamine nanoparticles with both organic antifouling and antibacterial properties. Desalination 326:69–76. https://doi.org/10.1016/j.desal.2013.07.018

[13] Wei T, Tang Z, Yu Q, Chen H (2017) Smart antibacterial surfaces with switchable bacteria-killing and bacteria-releasing capabilities. ACS Appl Mater Interfaces 9:37511–37523

[14] Sun G, Worley SD (2005) Chemistry of durable and regenerable biocidal textiles. J Chem Educ 82:60

[15] Dong A, Wang YJ, Gao Y et al (2017) Chemical insights into antibacterial N-Halamines. Chem Rev 117:4806–4862. https://doi.org/10.1021/acs.chemrev.6b00687

[16] Hui F, Debiemme-Chouvy C (2013) Antimicrobial N-halamine polymers and coatings: a review of their synthesis, characterization, and applications. Biomacromol 14:585–601. https://doi.org/10.1021/bm301980q

[17] Cerkez I, Kocer HB, Worley SD et al (2012) N-halamine copolymers for biocidal coatings. React Funct Polym 72:673–679. https://doi.org/10.1016/j.reactfunctpolym.2012.06.018

[18] Guillen GR, Pan Y, Li M, Hoek EMV (2011) Preparation and characterization of membranes formed by nonsolvent induced phase separation: a review. Ind Eng Chem Res 50:3798–3817. https://doi.org/10.1021/ie101928r

[19] Zhao C, Xue J, Ran F, Sun S (2013) Modification of polyethersulfone membranes-a review of methods. Prog Mater Sci 58:76–150. https://doi.org/10.1016/j.pmatsci.2012.07.002

[20] Issac MN, Kandasubramanian B (2020) Review of manufacturing three-dimensional-printed membranes for water treatment. Environ Sci Pollut Res 27:36091–36108. https://doi.org/10.1007/s11356-020-09452-2

[21] Thiam BG, El Magri A, Vanaei HR, Vaudreuil S (2022) 3D printed and conventional membranes–a review. Polymers (Basel) 14:1023. https://doi.org/10.3390/polym14051023

[22] Luelf T, Rall D, Wypysek D et al (2018) 3D-printed rotating spinnerets create membranes with a twist. J Membr Sci 555:7–19. https://doi.org/10.1016/j.memsci.2018.03.026

[23] Mullins N, Babamova I, de Lannoy CF, Latulippe DR (2024) Low-cost automated flat-sheet membrane casting: an open-source, advanced manufacturing approach. J Membr Sci Lett 4:100075. https://doi.org/10.1016/j.memlet.2024.100075

[24] Kocer HB, Worley SD, Broughton RM, Huang TS (2011) A novel N-halamine acrylamide monomer and its copolymers for antimicrobial coatings. React Funct Polym 71:561–568. https://doi.org/10.1016/j.reactfunctpolym.2011.02.002

[25] Vatanpour V, Madaeni SS, Moradian R et al (2012) Novel antibifouling nanofiltration polyethersulfone membrane fabricated from embedding TiO_2 coated multiwalled carbon nanotubes. Sep Purif Technol 90:69–82

[26] Zinadini S, Zinatizadeh AA, Rahimi M et al (2014) Preparation of a novel antifouling mixed matrix PES membrane by embedding graphene oxide nanoplates. J Memb Sci 453:292–301

[27] Hamid NAA, Ismail AF, Matsuura T et al (2011) Morphological and separation performance study of polysulfone/titanium dioxide (PSF/TiO_2) ultrafiltration membranes for humic acid removal. Desalination 273:85–92

[28] Pal Singh Chauhan N (2019) Biocidal polymers. Biocidal Polym 4:1–342. https://doi.org/10.1515/9783110639131

[29] Gzara L, Rehan ZA, Simone S et al (2017) Tailoring PES membrane morphology and properties via selected preparation parameters. J Polym Eng 37:69–81. https://doi.org/10.1515/polyeng-2015-0419

[30] Radovanovic P, Thiel SW, Hwang ST (1992) Formation of asymmetric polysulfone membranes by immersion precipitation. Part II. The effects of casting solution and gelation bath compositions on membrane structure and skin formation. J Memb Sci 65:231–246. https://doi.org/10.1016/0376-7388(92)87025-S

[31] Ding J, Wan Y, Zou Y et al (2023) Removal of membrane fouling and control of halogenated by-products by a combined cleaning process with peroxides and sodium hypochlorite. Water 15:2498

[32] Porcelli N, Judd S (2010) Chemical cleaning of potable water membranes: a review. Sep Purif Technol 71:137–143

[33] Puspitasari V, Granville A, Le-Clech P, Chen V (2010) Cleaning and ageing effect of sodium hypochlorite on polyvinylidene fluoride (PVDF) membrane. Sep Purif Technol 72:301–308

[34] Demirci F, Aydın A, Orhan M, Koçer HB (2022) Production of ultrafiltration membranes exhibiting antibacterial properties by the incorporation of novel N-halamine copolymers. J Appl Polym Sci 139:e52727. https://doi.org/10.1002/app.52727

[35] Wang H, Wang ZM, Yan X et al (2017) Novel organic-inorganic hybrid polyvinylidene fluoride ultrafiltration membranes with antifouling and antibacterial properties by embedding N-halamine functionalized silica nanospheres. J Ind Eng Chem 52:295–304. https://doi.org/10.1016/j.jiec.2017.03.059

[36] Smolders CA, Reuvers AJ, Boom RM, Wienk IM (1992) Microstructures in phase-inversion membranes. Part 1. Formation of macrovoids. J Membr Sci 73:259–275. https://doi.org/10.1016/0376-7388(92)80134-6

[37] Van De Witte P, Dijkstra PJ, Van Den Berg JWA, Feijen J (1996) Phase separation processes in polymer solutions in relation to membrane formation. J Membr Sci 117:1–31. https://doi.org/10.1016/0376-7388(96)00088-9

[38] Wen Y, Yuan J, Ma X et al (2019) Polymeric nanocomposite membranes for water treatment: a review. Environ Chem Lett 17:1539–1551

[39] Arkhangelsky E, Kuzmenko D, Gitis V (2007) Impact of chemical cleaning on properties and functioning of polyethersulfone membranes. J Membr Sci 305:176–184

[40] Wienk IM, Meuleman EEB, Borneman Z et al (1995) Chemical treatment of membranes of a polymer blend: mechanism of the reaction of hypochlorite with poly (vinyl pyrrolidone). J Polym Sci A Polym Chem 33:49–54

[41] Chakrabarty B, Ghoshal AK, Purkait MK (2008) Effect of molecular weight of PEG on membrane morphology and transport properties. J Membr Sci 309:209–221. https://doi.org/10.1016/j.memsci.2007.10.027

[42] Singh S, Khulbe KC, Matsuura T, Ramamurthy P (1998) Membrane characterization by solute transport and atomic force microscopy. J Membr Sci 142:111–127

[43] Fane AG, Wang R, Jia Y (2010) Membrane technology: past, present and future. In: Membrane and desalination technologies. Springer, pp 1–45

[44] Wijmans JG, Baker RW (1995) The solution-diffusion model: a review. J Membr Sci 107:1–21

[45] Okoro HK, Ndlwana L, Ikhile MI et al (2021) Hyperbranched polyethylenimine-modified polyethersulfone (HPEI/PES) and nAg@HPEI/PES membranes with enhanced ultrafiltration, antibacterial, and antifouling properties. Heliyon 7:523. https://doi.org/10.1016/j.heliyon.2021.e07961

[46] Rana D, Matsuura T (2010) Surface modifications for antifouling membranes. Chem Rev 110:2448–2471. https://doi.org/10.1021/cr800208y

[47] Gumbi NN, Hu M, Mamba BB et al (2018) Macrovoid-free PES/SPSf/O-MWCNT ultrafiltration membranes with improved mechanical strength, antifouling and antibacterial properties. J Membr Sci 566:288–300. https://doi.org/10.1016/j.memsci.2018.09.009

[48] Tan K, Obendorf SK (2007) Development of an antimicrobial microporous polyurethane membrane. J Membr Sci 289:199–209. https://doi.org/10.1016/j.memsci.2006.11.054

Publisher's Note Springer Nature remains neutral with regard to jurisdictional claims in published maps and institutional affiliations.